Monthly Notices of the ROYAL ASTRONOMICAL SOCIETY

MNRAS **518,** 2273–2286 (2023) https://doi.org/10.1093/mnras/stac2966
Advance Access publication 2022 October 18

Magnetic field evolution in cosmic filaments with LOFAR data

E. Carretti [1]★ S. P. O'Sullivan [2] V. Vacca [3] F. Vazza [4,1,5] C. Gheller,[1] T. Vernstrom [6] and A. Bonafede[4,1]

[1]*INAF, Istituto di Radioastronomia, Via Gobetti 101, I-40129 Bologna, Italy*
[2]*School of Physical Sciences and Centre for Astrophysics and Relativity, Dublin City University, Glasnevin D09 W6Y4, Ireland*
[3]*INAF, Osservatorio Astronomico di Cagliari, Via della Scienza 5, I-09047 Selargius (CA), Italy*
[4]*Dipartimento di Fisica e Astronomia, Universitá di Bologna, via Gobetti 93/2, I-40122 Bologna, Italy*
[5]*Hamburger Sternwarte, University of Hamburg, Gojenbergsweg 112, D-21029 Hamburg, Germany*
[6]*ICRAR, The University of Western Australia, 35 Stirling Hw, 6009 Crawley, Australia*

Accepted 2022 October 10. Received 2022 October 9; in original form 2022 July 6

ABSTRACT

Measuring the magnetic field in cosmic filaments reveals how the Universe is magnetized and the process that magnetized it. Using the Rotation Measures (RM) at 144 MHz from the LoTSS DR2 data, we analyse the rms of the RM extragalactic component as a function of redshift to investigate the evolution with redshift of the magnetic field in filaments. From previous results, we find that the extragalactic term of the RM rms at 144 MHz is dominated by the contribution from filaments (more than 90 per cent). Including an error term to account for the minor contribution local to the sources, we fit the data with a model of the physical filament magnetic field, evolving as $B_f = B_{f,0}\,(1+z)^{\alpha}$ and with a density drawn from cosmological simulations of five magnetogenesis scenarios. We find that the best-fitting slope is in the range $\alpha = [-0.2, 0.1]$ with uncertainty of $\sigma_\alpha = 0.4$–0.5, which is consistent with no evolution. The comoving field decreases with redshift with a slope of $\gamma = \alpha - 2 = [-2.2, -1.9]$. The mean field strength at $z = 0$ is in the range $B_{f,0} = 39$–84 nG. For a typical filament gas overdensity of $\delta_g = 10$ the filament field strength at $z = 0$ is in the range $B^{10}_{f,0} = 8$–26 nG. A primordial stochastic magnetic field model with initial comoving field of $B_{\rm Mpc} = 0.04$–0.11 nG is favoured. The primordial uniform field model is rejected.

Key words: magnetic fields – polarization – methods: statistical – intergalactic medium – large-scale structure of Universe.

1 INTRODUCTION

The evolution with cosmic time of the magnetic field is essential to understand how the present Universe is magnetized and the process of magnetogenesis (e.g. Subramanian 2016; Arámburo-García et al. 2021; Vazza et al. 2021b). Cosmic web filaments are a sweet spot for this, for they are not yet as processed by cosmic evolution as galaxy clusters are, thus preserving the signature of the initial magnetogenesis scenario (e.g. Vazza et al. 2017, 2021a, b; Mtchedlidze et al. 2022), while also possessing stronger fields than in voids, which makes their detection easier. Magnetogenesis scenarios can be broadly subdivided into primordial, where the field is generated either during Inflation or in some early phase-transition before the recombination (e.g. Turner & Widrow 1988; Kronberg 1994; Paoletti & Finelli 2019; Pomakov et al. 2022), and late, where the field is generated at low redshift by dynamo amplification or astrophysical sources that inject it in the intergalactic medium (IGM) as magnetic bubbles (e.g. Kronberg 1994; Bertone, Vogt & Enßlin 2006; Vazza et al. 2017).

The Rotation Measure (RM) of extragalactic sources measures the magnetic field component along the line of sight weighted by the free-electron number density and integrated along the entire line of sight. It is a powerful tool to investigate magnetic field properties of the Galaxy (e.g. Jansson & Farrar 2012; Dickey et al. 2022), the environment local to the source (e.g. Kronberg et al. 2008), or the intervening IGM between the source and the observer (e.g. Vernstrom et al. 2019; O'Sullivan et al. 2020).

The detection of the radio emission of cosmic filaments and of their magnetic field through synchrotron emission and RM was the subject of intense research in the past few years. Upper limits were found with different approaches: cross-correlating large radio maps with the large-scale galaxy distribution (Brown et al. 2017; Vernstrom et al. 2017); analysing RMs of giant radio galaxies (O'Sullivan et al. 2019; Stuardi et al. 2020); cross-correlating RMs with the galaxy distribution (Amaral, Vernstrom & Gaensler 2021); simulations constrained by observations or non-detections (Vacca et al. 2018; Locatelli et al. 2021). Intracluster bridges of radio emission were detected in a few galaxy clusters[1] (e.g. Kim et al. 1989; Brown & Rudnick 2011; Bonafede et al. 2022; de Gasperin et al. 2022). A detection of the synchrotron emission from an intercluster bridge connecting close pairs of merging clusters was obtained by Govoni et al. (2019) (see also Botteon et al. 2020; Venturi et al. 2022),

★ E-mail: carretti@ira.inaf.it

[1]Kim et al. (1989) proposed that the structure they found, stretching out of the Coma galaxy cluster halo, was an intercluster bridge connecting the Coma cluster to the cluster A1367. Later observations have shown it is an intracluster bridge in the Coma cluster connecting the halo to the SW relic (e.g. Brown & Rudnick 2011; Bonafede et al. 2022).

© 2022 The Author(s)
Published by Oxford University Press on behalf of Royal Astronomical Society

Downloaded from https://academic.oup.com/mnras/article/518/2/2273/6762929 by INAF Trieste (Osservatorio Astronomico di Trieste) user on 30 January 2023

establishing the presence of magnetic fields in the IGM beyond cluster outskirts. Vernstrom et al. (2021) and Carretti et al. (2022) made a further step ahead, first detecting fields of the general, weaker filaments of the cosmic web of 30–60 nG and ≈30 nG, through stacking of synchrotron emission and measuring the RM evolution with redshift, respectively.

The evolution with redshift of the RM and average magnetic field of the Universe were investigated by several authors (e.g. Xu & Han 2014 and references therein and in Carretti et al. 2022), but hampered by the separation of local and IGM components. Pomakov et al. (2022) separated the IGM term using the differential RM of close pairs of galaxies from the same, low frequency RM catalogue we used in Paper I, and measured the evolution with redshift of the average magnetic field of the Universe.

In Carretti et al. (2022), hereafter Paper I, we used the RM catalogue at 144 MHz (O'Sullivan et al., submitted) derived from LoTSS DR2 (LOFAR Two-metre Sky Survey Data Release 2; Shimwell et al. 2017, 2019, 2022) data to measure the behaviour of RM in redshift bins out to $z = 2$, after subtracting off the Galactic contribution, and the behaviour versus the fractional polarization p. We found that the former is consistent with no evolution, and the latter is flat with p. After a comparison with the RM and p measured at 1.4 GHz of the same sources, we found that an IGM origin of the RMs is favoured and estimated a magnetic field in filaments of ≈30 nG, as reported above. We assumed no evolution for magnetic field and electron number density, however, except assuming the mean electron number density at $z = 0.7$.

This work is a follow-up of Paper I, aimed at investigating the evolution with redshift of the magnetic field in cosmic filaments, adding in the evolution of the quantities involved. It is conducted within the Magnetism Key Science Project (MKSP) of LOFAR and uses the RM catalogue at 144 MHz employed in Paper I (O'Sullivan et al., submitted), which is derived from LoTSS DR2 (Shimwell et al. 2022) Stokes Q and U data cubes in a collaborative effort between the LOFAR Surveys Key Science Project[2] and the MKSP. It also uses dedicated cosmological magnetohydrodynamical (MHD) simulations of a set of magnetogenesis scenarios, to draw realistic density distributions from and to compare our results with. We find the RM evolution with redshift a powerful way to discriminate between cosmological magnetogenesis models.

This paper is organized as follows. Section 2 describes the RM data and the RM rms in redshift bins out to $z = 3$, after subtracting off the Galactic contribution. Section 3 describes the MHD simulations of the magnetogenesis scenarios we used for this work. Section 4 contains our analysis of the evolution with redshift of the magnetic field in cosmic filaments, including best fits to the data, considerations on the environment where the low-frequency RMs are produced, and estimates of the predictions of the magnetogenesis scenarios we considered. Finally, Sections 5 and 6 present our discussion and conclusions, with a comparison of our results with the magnetogenesis scenarios we considered.

Throughout the paper we assume the flat ΛCDM cosmological model assumed in the simulations of Section 3, with $H_0 = 67.8$ km s^{-1} Mpc^{-1}, $\Omega_M = 0.308$, $\Omega_\Lambda = 0.692$, $\Omega_b = 0.0468$, and $\sigma_8 = 0.815$ (Planck Collaboration XIII 2016). Errors refer to 1-sigma uncertainties.

[2]https://lofar-surveys.org/

2 RM DATA

2.1 LoTSS DR2 RM catalogue

This work is based on the RM catalogue derived from the LoTSS DR2 survey using its Stokes Q and U data cubes (O'Sullivan et al., submitted). Here we report the main catalogue features relevant to this work and refer to the description paper for full details. It consists of 2461 RMs detected, over 5720 deg^2, in the frequency range 120–168 MHz with channels of width of 97.6 kHz, and angular resolution of 20 arcsec. RMs were obtained using RM synthesis (Burn 1966; Brentjens & de Bruyn 2005). The RM error budget is dominated by ionospheric RM correction residuals that can be as large as 0.1–0.3 rad m^{-2} (Sotomayor-Beltran et al. 2013; Porayko et al. 2019). In this data set it is estimated to be ≈0.05 rad m^{-2} (O'Sullivan et al., submitted). A total number of 1949 sources had a positive cross-match with redshift catalogues, 1046 of which are spectroscopic redshifts.

We did not use photometric redshifts of the identified sources because of their median error of $\sigma_{z,\mathrm{phot}} \approx 0.1$, comparable to or larger than the redshift bin width used here, and kept sources with spectroscopic redshift only. A Galactic cut of $|b| > 25^\circ$ was applied to exclude the region with highest Galactic RM values. The median redshift is ≈0.5 and only a handful of sources have redshift $z > 3$ (see fig. 1 of Paper I for the redshift distribution). We limited our analysis to $z < 3$, which gave our final sample of 1014 objects.

2.2 Behaviour of RM dispersion

The estimate of the evolution with redshift of the RM extragalactic component is done as for Paper I, except it is stretched out to $z = 3$ and the numbers of bins is increased by ≈4 times.

The RM of an extragalactic source is a combination of a Galactic component (GRM), an extragalactic term, either local to the source or the IGM intervening between the source and the observer, and the instrumental noise:

$$\mathrm{RM} = \mathrm{GRM} + \mathrm{RM}_{\mathrm{local}} + \mathrm{RM}_{\mathrm{IGM}} + \mathrm{RM}_{\mathrm{noise}} . \quad (1)$$

The local term usually is dominated by the environment around the source, such as the intracluster medium of a galaxy cluster (e.g. Laing et al. 2008).

The extragalactic component is obtained by subtracting off the Galactic term:

$$\mathrm{RRM} = \mathrm{RM} - \mathrm{GRM} \quad (2)$$

that we call the Residual RM (RRM).

Following Paper I, we estimated the GRM at each source position from the Galactic RM map by Hutschenreuter et al. (2022) as the median of a 1-degree diameter disc centred at the source. We refer to Paper I for details and motivations. The result is shown in Figs 1 and 2 that report the RRMs of the two fields of the sample. The GRM error of each source is estimated by bootstrapping, which also captures the GRM variations within the 1-degree disc.

We then computed the dispersion of the RRM values $<\mathrm{RRM}^2>^{1/2}$ (hereafter RRM rms) in redshift bins with the same number of sources per bin, as for Paper I. The quadratic mean of the GRM errors and of the measurement noise of the sources in each bin

Downloaded from https://academic.oup.com/mnras/article/518/2/2273/6762929 by INAF Trieste (Osservatorio Astronomico di Trieste) user on 30 January 2023

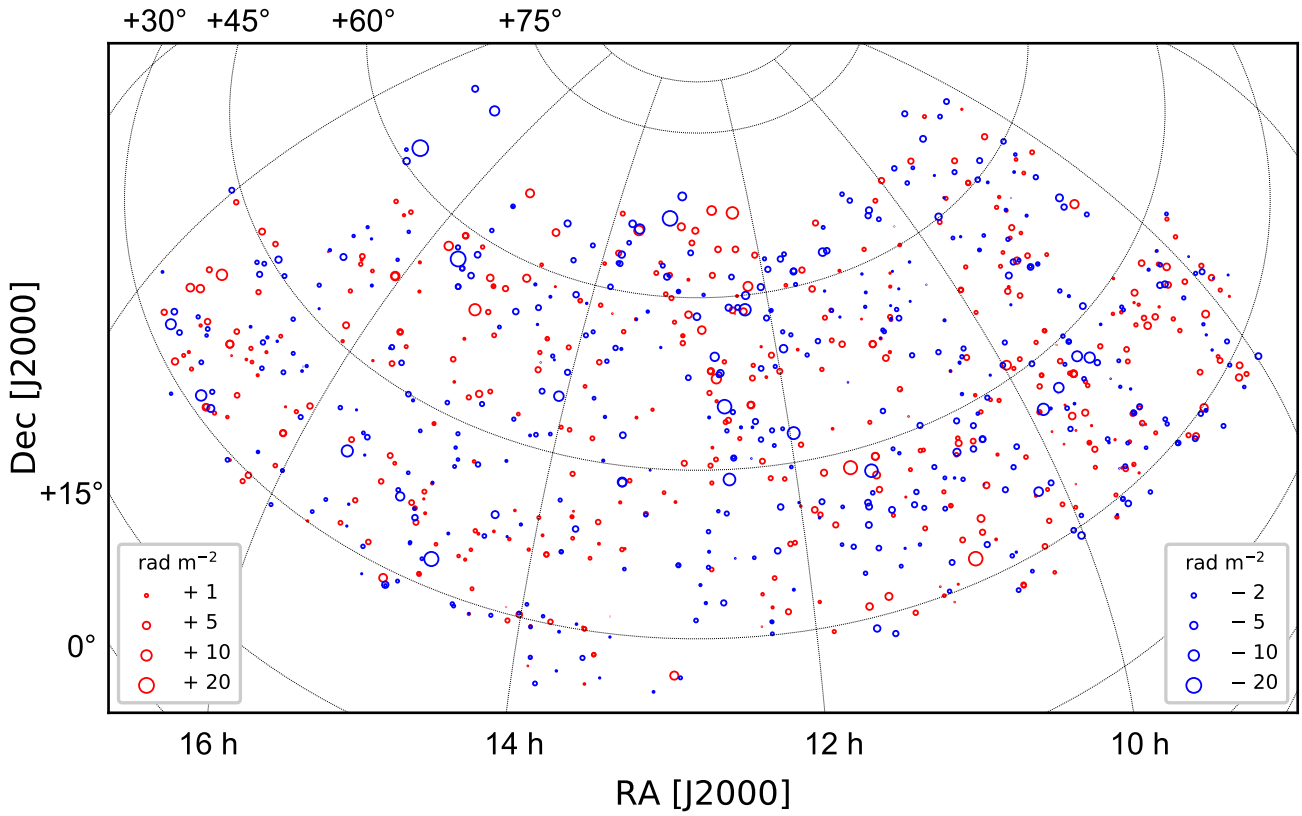


Figure 1. Sky distribution of the RRM sample used in the analysis. The field of the LoTSS DR2 survey centred at RA = 13h is shown.

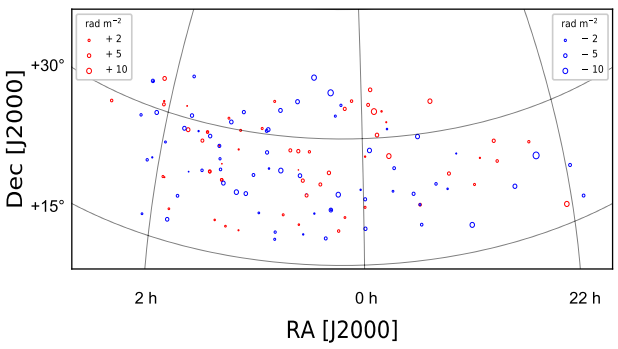


Figure 2. As for Fig. 1, except the field centred at RA = 0h is shown.

were quadratically subtracted off to remove their bias.[3] We excluded outliers, only keeping RRMs witin 2-sigma, as for Paper I.

The result is shown in Fig. 3 for two cases, 60 and 15 sources per bin, which differ in the number of bins (17 and 68, respectively) and the uncertainty per bin (mean of 0.21 and 0.35 rad m^{-2}). The error is estimated by bootstrapping. Both cases are consistent with no evolution with redshift, the slope of a linear regression is 0.22 ± 0.17 rad m^{-2} and 0.24 ± 0.20 rad m^{-2} for the two cases. There is a marginal increase, but at less than 2-sigma significance.

3 COSMOLOGICAL MHD SIMULATIONS

We used the cosmological magnetohydrodynamical code ENZO[4] to produce new ΛCDM simulations of a volume of ≈(85 Mpc)^3 (comoving) sampled with a static grid of 512^3 cells, giving a constant spatial resolution of 166 kpc per cell and a constant mass resolution of $6.48 \times 10^8\,M_\odot$ per dark matter particle. These simulations are qualitatively similar to those analysed in Vazza et al. (2017), with a few updates, also motivated by the findings of our recent work in Pomakov et al. (2022). First, in this suite of simulations, radiative gas cooling is included in all models, which moderately increases the level of gas clumping in cosmic filaments. Furthermore, we explored additional models of magnetic fields, including an inflationary primordial model following Vazza et al. (2021b), and a mixed (astrophysical and primordial) model. Lastly, we produced synthetic lines of sight out to a larger redshift ($z = 3$, as opposed to $z = 2$ in Pomakov et al. 2022) using a much larger number of snapshots finely spaced in time, as compared to earlier work, to monitor evolutionary trends with redshift in a more accurate way. These simulations are used to estimate the magnetic field in cosmic filaments instead of the general IGM. Similar to previous projects (e.g. Vazza et al. 2017), we produced different scenarios (five in this case) for the origin and evolution of extragalactic magnetic fields:

[3]The square of the measured RRM rms is $< \mathrm{RRM_{mes}}^2 > = < \mathrm{RRM}^2 > + \sigma^2_{\mathrm{GRM}} + \sigma^2_{\mathrm{noise}}$, where σ^2_{GRM} and $\sigma^2_{\mathrm{noise}}$ are the means of the variances of GRM and measurement noise.

[4]http://enzo-project.org

Downloaded from https://academic.oup.com/mnras/article/518/2/2273/6762929 by INAF Trieste (Osservatorio Astronomico di Trieste) user on 30 January 2023

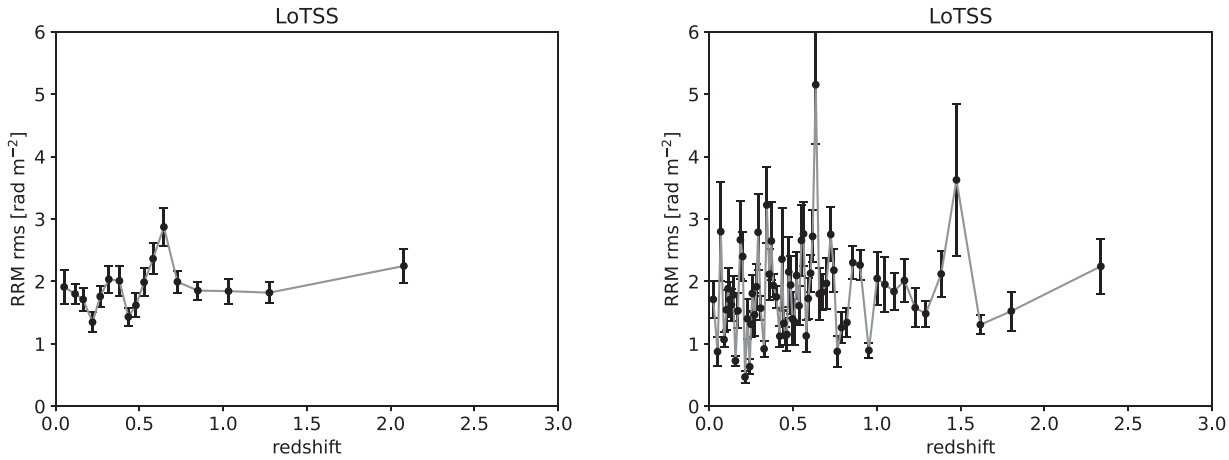


Figure 3. RRM rms in redshift bins with the same number of sources, 60 (left-hand panel) and 15 (right-hand panel).

(i) *'primordial uniform'*: a primordial uniform volume-filling comoving magnetic field $B_0 = 0.1$ nG initialized at the beginning of the simulation ($z = 40$);

(ii) *'primordial stochastic'*: a tangled primordial magnetic field, with fields scale dependence described by a power-law spectrum: $P_B(k) = P_{B0}k^{\alpha_s}$ characterized by a constant spectral index and an amplitude, commonly referred after smoothing the fields within a scale $\lambda = 1$ Mpc, using the same approach of Vazza et al. (2021b). In this work we assumed an initial 'blue' spectrum with $\alpha_s = 1.0$ and $B_{\rm Mpc} = 0.042$ nG (comoving), based on the recent constraints from the combined analysis of the Cosmic Microwave Background with different instruments by Paoletti & Finelli (2019). We selected this value of α_s from the best constraint provided by previous observational tests (Vazza et al. 2021a).

(iii) *'dynamo'*: a uniform initial seed magnetic field of $B_0 = 10^{-11}$ nG (comoving) that can be amplified through 'sub-grid' dynamo amplification computed at run-time, which allows the estimation of the hypothetical maximum contribution of a dynamo in low density environments (see Ryu et al. 2008), where it would be lost due to finite resolution effects (see Vazza et al. 2017, for more details);

(iv) *'astroph'*: a model in which the magnetic field is released in the form of magnetic loops from overdense regions of the simulation, whenever AGN feedback is triggered by local gas overcooling. To maximize the plausible combined effect of star formation driven winds, and AGN feedback, we assumed a large, average of 50 per cent conversion efficiency between the energetics of each single feedback event, and the release of magnetized bipolar outflows in galaxies, starting from $z = 4$ and down to $z = 0$. This field is added to a negligible uniform initial seed field of $B_0 = 10^{-11}$ nG (comoving), leading to 'magnetic bubbles' correlated with haloes in the simulated volume.

(v) *'primordial + astroph'*: a model that combines the same magnetization scheme of the 'astroph' model, but it also assumes a primordial uniform magnetic field of $B_0 = 0.01$ nG initialized at the beginning of the simulation.

As an important improvement over our previous work, in these simulations we include the effect of radiative (equilibrium) cooling on baryon gas, assuming for simplicity a primordial chemical composition. This is motivated because a recent analysis of previous runs has shown that the density statistics, even in the mild density regime of the cosmic web, is more realistic when cooling is included since the start, compared to simpler non-radiative runs (Pomakov et al. 2022).

The adopted cosmological parameters are as for Section 1. The production of these new simulations was motivated in order to produce long lines of sight (LOS) with a finely sampled redshift evolution of gas and magnetic field quantities from $z = 3$ to $z = 0$, which was not available in existing simulations.

To allow a comparison with the observed RM, we generated 100 LOS through each simulated volume, with information of gas density and 3D magnetic field from $z = 3$ to $z = 0$. Each LOS is ≈6.1 comoving Gpc long and was produced by replicating the simulated volume 72 times, using 21 snapshots saved at nearly equally spaced redshifts, and by randomly varying the volume-to-volume crossing position for a total of ≈36 800 cells for each simulated LOS.

We note that a second data set of cosmological simulations, already extensively presented elsewhere (e.g. Vazza et al. 2017; Gheller & Vazza 2019), was used to estimate the evolution of the diameter of filaments with redshift in Section 4.2, as catalogues of thousands of filaments were already available for this. The physical prescriptions in these runs were very similar to those used in our main simulations, and additional differences in the adopted numerical resolution are expected to play no role in the analysis of filament diameters derived there.

4 EVOLUTION WITH REDSHIFT OF FILAMENT MAGNETIC FIELDS

In this section, we investigate whether the RRM rms measured at different redshifts can constrain the evolution of the magnetic field in cosmic filaments. We start with considerations on the environment that generates the RRM of our sample at 144 MHz. Then, we do a simple, semi-analytical analysis assuming simple evolution with redshift of cosmic quantities. We then carry out a more accurate analysis taking a more realistic gas density distribution from cosmological MHD simulations, either assuming a constant field strength or having it related to the gas density. We assume that the gas is 100 per cent ionized, which is a safe assumption out to $z = 5.3$ (Bosman et al. 2022). Finally, we estimate the RRMs predicted by the cosmological models for a comparison with the observational results.

Downloaded from https://academic.oup.com/mnras/article/518/2/2273/6762929 by INAF Trieste (Osservatorio Astronomico di Trieste) user on 30 January 2023

4.1 Environment

In Paper I, we found that an IGM origin is favoured for the RRMs of our sample at low frequency, instead of local to the source. This was inferred from the behaviour of the RRM with fractional polarization (p) and redshift, and the evolution of p with redshift. We also found that these sources reside far from galaxy clusters at a projected distance that peaks at $\approx 5\,R_{200}$ that is well beyond a cluster virial radius $R_{100} \approx 1.36\,R_{200}$ (Reiprich et al. 2014). We repeated the analysis of Paper I and found that 7 per cent of the sources have a projected distance from clusters closer than R_{100}, which means that only $\approx 0.07^{3/2} = 2$ per cent of them are estimated to have a 3D separation shorter than R_{100} (see Appendix A). R_{100} is the distance within which the mean density of the galaxy cluster is $100\times$ the critical density of the Universe (ρ_c). From simulations, we find this corresponds to a local overdensity of $\rho/\rho_c \approx 50$ or, in terms of mean matter density $<\rho_M>$, $\rho_M/<\rho_M> \approx 160$, according to our cosmology.

This shows that the polarized sources are not embedded in galaxy cluster environments at these frequencies. We also checked that intervening clusters are far from the LOS of our sources, with a similar analysis to that of Paper I. For each source of our sample, we searched for the intervening galaxy cluster with the smallest projected separation from the LOS in R_{100} units. We used the galaxy cluster catalogue of Wen & Han (2015) that contains 158 103 records in the redshift range of 0.05–0.75, either spectroscopic or photometric, with an error of up to 0.018. The cluster masses are as low as $2 \times 10^{12}\,\mathrm{M}_\odot$ and the sample is 95 per cent complete for masses larger than $10^{14}\,\mathrm{M}_\odot$. For each source at redshift z_s, we searched for the smallest projected separation to the LOS of the clusters at redshift $z_{\rm gc} < z_s - 0.036$ (2-sigma uncertainty). We found that 5.2 and 8.9 per cent of the sources have an LOS that passes at a distance from a cluster closer than R_{200} and R_{100}, respectively. The median minimum projected separation is 3.5 R_{200}, or 2.6 R_{100}, which is well beyond the cluster environment. If we restrict the search to clusters of masses larger than $10^{14}\,\mathrm{M}_\odot$, which are expected to give the largest effects, those fractions drop to 2.4 and 4.9 per cent for R_{200} and R_{100}. These results are comparable to those of the analysis on the closest galaxy cluster separation, and the same considerations hold. Only sources within the galaxy cluster catalogue footprint and in its redshift range were used, providing 739 sources for this analysis.

Pomakov et al. (2022) estimated the differential RRM of close pairs of sources from the same LoTSS RM catalogue at 144 MHz we use here, either random pairs (rp: sources apparently close but physically separated and at different redshift) or physical pairs (pp: two components of the same source, such as two lobes of a radio galaxy, that are at the same distance). Differential RMs have been employed to investigate either the magnetic field in the IGM (e.g. Vernstrom et al. 2019) or the ICM in galaxy clusters (e.g. Xu & Han 2022). For the latter the pp are used and it is best applied at higher frequencies where the polarized sources can populate clusters (see above). The differential RRM of a random pair has three contributions: the IGM intervening the two sources; their local environment; and a possible contamination from the residual GRM. Physical pair differential RRMs have two possible contributions: the environment local to the sources and the possible residual GRM. Those authors measured medians of differential $|\Delta\mathrm{RRM}|$ of $\langle|\Delta\mathrm{RRM_{rp}}|\rangle = 1.79 \pm 0.09$ rad m^{-2} and $\langle|\Delta\mathrm{RRM_{pp}}|\rangle = 0.70 \pm 0.08$ rad m^{-2} for random and physical pairs, from which we estimate single source rms of $<\mathrm{RRM^2_{rp}}>^{1/2} = 1.88 \pm 0.09$ rad m^{-2} and $<\mathrm{RRM^2_{pp}}>^{1/2} = 0.73 \pm 0.08$ rad m^{-2}, once we have corrected by 1.4826 to estimate rms from the median absolute deviation[5] and divided by $\sqrt{2}$ to get the single source rms. The former is in excellent agreement with our estimate in Paper I of 1.90 ± 0.05 that used single source RRMs.

To get an estimate of the sole IGM contribution we can quadratically subtract those two values, which gives $<\mathrm{RRM^2_{IGM}}>^{1/2} = 1.73 \pm 0.12$ rad m^{-2}. That is only 8 per cent smaller than the measured term that is thus largely dominated by the IGM RRMs. This is a further indication that our measured RRMs are mostly generated by the IGM and we will assume so in the rest of the paper. To account for the local origin contribution we add an error of 8 per cent to our RRM rms estimates.

We used the cosmological MHD simulations described in Section 3 to estimate the fraction of the IGM RRM that is from filaments and voids. For each cosmological model, we measured the RRM at each redshift out to $z = 3$ for each of the 100 LOS using density and magnetic field from the simulations and then computed the rms $<\mathrm{RRM^2_{IGM,sim}}>^{1/2}$. We only considered cells with density excess $\delta_M = \rho_M/<\rho_M> < 160$, to account for the fact that most of our sources are far from galaxy clusters (i.e. estimating the RRM rms of the entire IGM excluding clusters). We measured the $<\mathrm{RRM^2_{voids,sim}}>^{1/2}$ from voids with the same procedure, except we only considered cells with a gas density excess of $\delta_g = \rho_g/<\rho_g> < 1$, which is a conservative separation threshold between filaments and voids (Cautun et al. 2014; Vazza et al. 2015). We then computed the median of the ratio $<\mathrm{RRM^2_{voids,sim}}>^{1/2} / <\mathrm{RRM^2_{IGM,sim}}>^{1/2}$ for all models and we find that it is smaller than 0.013 (it ranges 1×10^{-3} to 0.013 depending on the model), for a fractional contribution of the voids to $<\mathrm{RRM^2_{IGM,sim}}>^{1/2}$ of less than 1×10^{-4}. From this, we can conclude that voids provide a negligible contribution to our sample RRMs that therefore mostly have an origin from cosmic filaments.

4.2 Semi-analytical analysis

The RRM of a source at redshift z is

$$\mathrm{RRM} = 0.812 \int_z^0 \frac{n_e(z') B_\parallel(z')}{(1+z')^2} \frac{\mathrm{d}l}{\mathrm{d}z'}\,\mathrm{d}z', \tag{3}$$

where the integration is performed from the source to the observer along the path length l (pc), n_e is the electron number density (cm^{-3}), and $B_\parallel$ is the magnetic field along the line of sight (μG), all referred to physical quantities.

In cosmic filaments the electron density is $n_{e,f} = K_f\,n_e$, where n_e is the average electron density of the Universe and K_f is the filament overdensity, that is $K_{f,0} = 10$ at $z = 0$ (Cautun et al. 2014; Vazza et al. 2015) and evolves as (Cautun et al. 2014, we derived this dependence from their fig. 25)

$$K_f \approx K_{f,0}\,(1+z)^{-0.75}. \tag{4}$$

Hence, the electron number density in a cosmic filament varies with redshift as

$$n_{e,f} = K_f\; n_{e,0}\;(1+z)^3\,, \tag{5}$$

where $n_{e,0}$ is the mean comoving (at $z = 0$) electron number density of the Universe, and the RRM of a source at redshift z by cosmic filaments intercepted by the source radiation is:

$$\mathrm{RRM_f} = 0.812\; K_{f,0}\; n_{e,0} \int_z^0 B_\parallel\,(1+z')^{0.25}\,\frac{\mathrm{d}l}{\mathrm{d}z'}\,\mathrm{d}z'. \tag{6}$$

[5]Possible in case of zero mean, as found in Paper I

Downloaded from https://academic.oup.com/mnras/article/518/2/2273/6762929 by INAF Trieste (Osservatorio Astronomico di Trieste) user on 30 January 2023

The medium can be assumed to be distributed in $N_f(z)$ filaments intercepted by the LOS out to redshift z, and equation (6) can be written as

$$\mathrm{RRM_f} = 0.812\ K_{f,0}\ n_{e,0} \sum_i^{N_f(z)} B_{\parallel,f,i}\ (1+z_i)^{0.25}\ l_f, \tag{7}$$

where $B_{\parallel,f,i}$ is $B_\parallel$ of a filament at redshit z_i and $l_f = (\pi/2)\ D$ is the typical path of the LOS through a filament, considering the typical width of a filament (D) corrected for the average inclination to the LOS of the filament (see Appendix B of Paper I). The typical width of a filament at $z = 0$ is $D_0 \approx 6$ Mpc (Aragón-Calvo, van de Weygaert & Jones 2010; Cautun et al. 2014; Galárraga-Espinosa et al. 2020). To estimate the evolution of D with redshift, we used the statistics of filaments already extracted in a suite of simulations produced elsewhere (Gheller & Vazza 2019), with the same numerical method and (nearly) physical prescriptions of the new simulations introduced in Section 3. We detected filaments at redshifts out to $z = 3$ using an excess density threshold criterion of $\delta = 10$ at $z = 0$ and decreasing with z following the growth rate of cosmic structures (see equation (B5) of Klypin, Trujillo-Gomez & Primack 2011) down to $\delta = 2.48$ at $z = 3$. The fit to the mean filament radius, weighted for the filament density, provides a dependence D (comoving) $\propto (1+z)^{-0.4}$ and in physical coordinates we can assume

$$l_f = l_{f,0}\ (1+z)^{-1.4}, \tag{8}$$

where $l_{f,0} = \pi/2\ D_0$.

If we express $B_{\parallel,f,i} = B_{f,i}\cos\theta$, where θ is the inclination of the filament field to the LOS that is uniformly distributed over 4π-sr, and B_f, i is the magnetic field strength of filaments at redshift z_i, the RRM rms over all LOS can be written as:

$$\left\langle \mathrm{RRM_f}^2 \right\rangle^{1/2} = 0.812\ K_{f,0}\, n_{e,0}\, l_{f,0} \sqrt{\sum_i^{N_f(z)} \frac{\left(B_{f,i}\,(1+z_i)^{-1.15}\right)^2}{3}} \tag{9}$$

We can assume that B_f follows a simple power law (see Pomakov et al. 2022)

$$B_f = B_{f,0}\ (1+z)^{\alpha}, \tag{10}$$

and, after defining

$$A_{f,0} = 0.812\ \frac{K_{f,0}\, n_{e,0}\, l_{f,0}}{\sqrt{3}}, \tag{11}$$

RRM_f rms becomes

$$\left\langle \mathrm{RRM_f}^2 \right\rangle^{1/2} = A_{f,0}\, B_{f,0} \sqrt{\sum_i^{N_f(z)} (1+z_i)^{2\alpha-2.3}} \tag{12}$$

and hence

$$\left\langle \mathrm{RRM_f}^2 \right\rangle^{1/2} = A_{f,0}\, B_{f,0} \sqrt{\sum_i^{N_f(z)} (1+z_i)^{2\alpha-2.3} \frac{\Delta N_f}{\Delta z} \Delta z} \tag{13}$$

that can be turned into an integral

$$\left\langle \mathrm{RRM_f}^2 \right\rangle^{1/2} = A_{f,0}\, B_{f,0} \sqrt{\int_0^z (1+z')^{2\alpha-2.3} \frac{\mathrm{d}N_f}{\mathrm{d}z'}\ \mathrm{d}z'}. \tag{14}$$

The number of filaments N_f is, to a good approximation, linear with z (see Paper I). We followed the same analysis of Paper I to estimate the number of filaments intercepted by the LOS of the sources of our RM catalogue. We used the filament catalogues by Chen et al. (2016) and Carrón Duque et al. (2022) and found the number of filaments intercepted by each of the RM catalogue sources that are in their footprint, and fit the distribution of N_f so obtained (Fig. 4). We assumed a filament width of 6 Mpc at $z = 0$ (Aragón-Calvo et al. 2010; Cautun et al. 2014; Galárraga-Espinosa et al. 2020), evolving with redshift as discussed above. Differing from Paper I, we did the analysis out to the max distance of the filament catalogues ($z = 2.2$), considered a width changing with redshift, and executed a linear fit, which gives

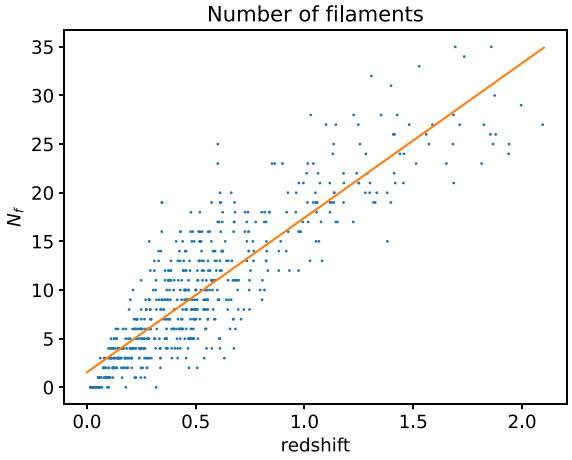


Figure 4. Number of filaments intercepted by each of our sources in the footprint of the filaments catalogues (dots). The best fit is also reported (solid line).

$$\begin{aligned} N_f &= N_0 + N_1\, z \\ N_0 &= 1.5 \\ N_1 &= 15.9 \end{aligned} \tag{15}$$

We do not have filament data beyond $z = 2.2$ and we extrapolate this relation out to $z = 3$.

Equation (14) thus becomes

$$\left\langle \mathrm{RRM}^2 \right\rangle^{1/2} = A_{f,0}\, N_1^{1/2}\, B_{f,0} \sqrt{\int_0^z (1+z')^{2\alpha-2.3}\ \mathrm{d}z'} \tag{16}$$

with solution

$$\left\langle \mathrm{RRM_f}^2 \right\rangle^{1/2} = \begin{cases} A_{f,0}\, N_1^{1/2}\, B_{f,0} \sqrt{\frac{(1+z)^{2\alpha-1.3}-1}{2\alpha-1.3}} & \text{for } \alpha \neq 0.65 \\ A_{f,0}\, N_1^{1/2}\, B_{f,0} \sqrt{\ln(1+z)} & \text{for } \alpha = 0.65 \end{cases} \tag{17}$$

As discussed in Section 4.1, a cosmic filament origin can be assumed for our RRM sample measured at 144 MHz with LOFAR. Hence, we fit the measured RRM rms to the function

$$\left\langle \mathrm{RRM}^2 \right\rangle^{1/2} = \frac{A_{rrm}}{(1+z)^2} + \left\langle \mathrm{RRM_f}^2 \right\rangle^{1/2}, \tag{18}$$

where besides the cosmic filament term RRM_f, we allow a constant RRM term, corrected for redshift, to account for a possible additional contribution different from filaments. This is motivated because the model RRM_f converges to zero at $z = 0$ while our measured RRMs do not. We use a Bayesian fit,[6] with priors of $B_{f,0} < 250$ nG (Locatelli et al. 2021), $B_{f,0} \geqq 0$, and $A_{rrm} \geqq 0$. The results are shown in Fig. 5 where we used the RRM rms computed in bins of 15 sources each.

[6] EMCEE package (Foreman-Mackey et al. 2013): https://pypi.org/project/emcee/

Downloaded from https://academic.oup.com/mnras/article/518/2/2273/6762929 by INAF Trieste (Osservatorio Astronomico di Trieste) user on 30 January 2023

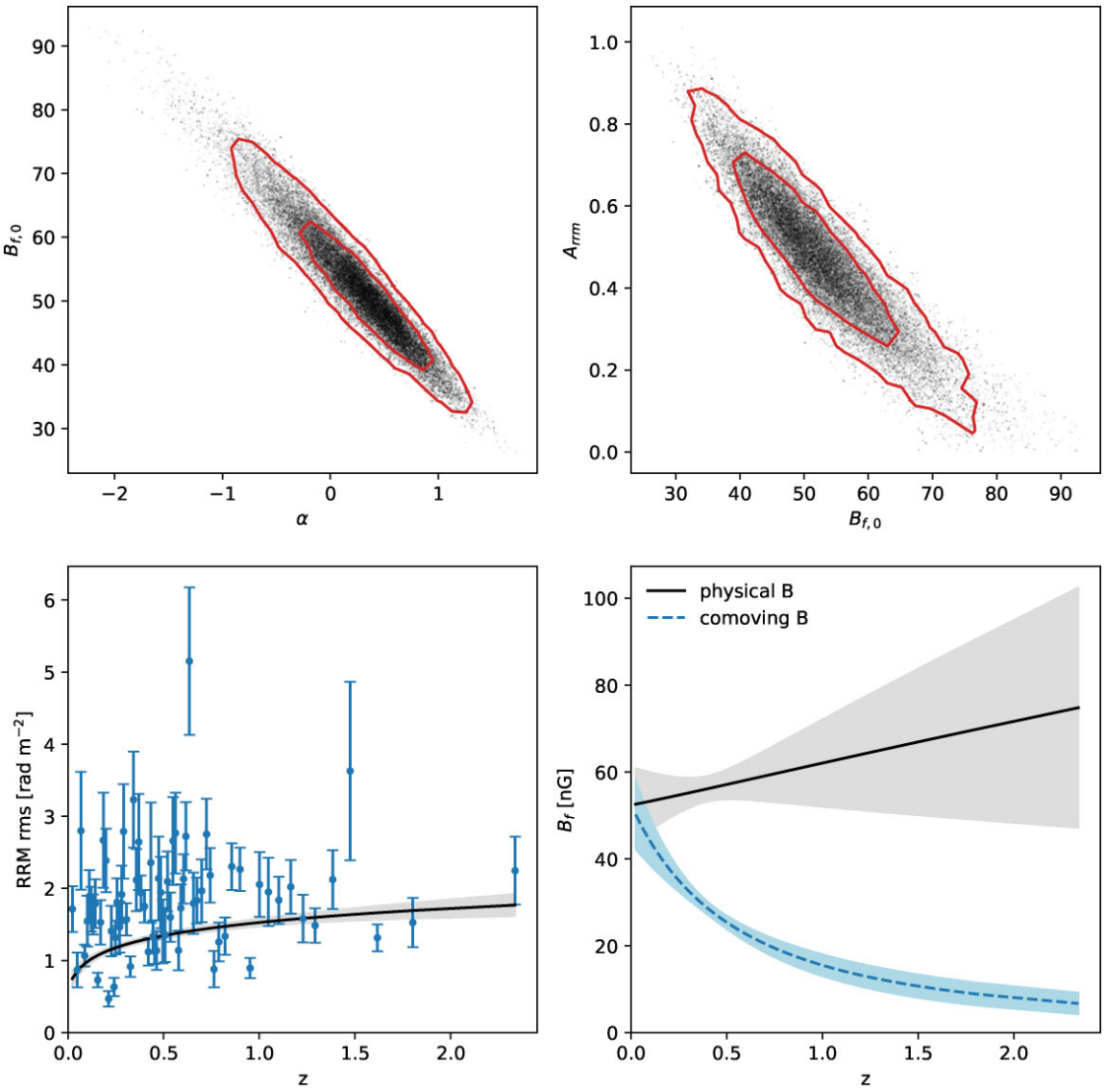


Figure 5. Best-fitting results of the semi-analytical model of equations (18) and (17) to the RRM rms computed with redshift bins of 15 sources per bin. Top left-hand panel and top right-hand panel: 2D distributions (dots), and 1-sigma and 2-sigma confidence level contours (solid lines) of the fit parameters α, $B_{f,0}$, and A_{rrm}. Bottom left-hand panel: RRM rms measured in redshift bins (circles) and best-fitting curve (solid) and its error range (grey-shaded area). Bottom right-hand panel: Evolution with redshift z of the best-fitting filament physical (solid line) and comoving magnetic field amplitude (dashed). The error range is also shown (shaded areas).

The 2D confidence level contours of the parameters, the best-fitting model, and the resulting evolution of B_f with redshift are shown. The best-fitting results (Table 1) give a filament magnetic field with a slope $\alpha = 0.2 \pm 0.5$ that is consistent with no evolution with redshift, as also shown in Fig. 5, bottom right-hand panel, and with an amplitude at $z = 0$ of $B_{f,0} = 52 \pm 9$ nG. The latter can be also written as:

$$B_{f,0} = (52 \pm 9) \left(\frac{6 \text{ Mpc}}{D_0} \right) \text{ nG} \tag{19}$$

that shows the dependence of $B_{f,0}$ on the filament width (these two parameters are inversely proportional, see equation 17).

Assuming the magnetic field is frozen to the plasma, the magnetic field goes as $n_e^{2/3}$ and thus $B_f = B_{f,c}\,(1+z)^2$, where $B_{f,c}$ is the comoving magnetic field in filaments that, according to our model for B_f, varies with z as

$$B_{f,c}(z) = B_{f,0}\,(1+z)^{\gamma} \quad \text{with } \gamma = \alpha - 2. \tag{20}$$

From the results of our fit, hence, we get $\gamma = -1.8 \pm 0.5$, which gives a comoving magnetic field in filaments that significantly evolves, decreasing with redshift. The behaviour of the comoving field is shown in Fig. 5, bottom right-hand panel.

We also run the fit to the RRM rms computed with a set of larger redshift bins (60 sources each). The results, shown in Table 1, are consistent with those obtained with smaller bins, albeit with larger errors.

4.3 Analysis with densities from cosmological simulations

The semi-analytical approach is powerful and gives an insight into the terms at play, but it has limitations. Those most obvious are the gas density assumed to follow that of the dark matter and the

Downloaded from https://academic.oup.com/mnras/article/518/2/2273/6762929 by INAF Trieste (Osservatorio Astronomico di Trieste) user on 30 January 2023

Table 1. Best-fitting parameters of the filament magnetic field evolution with redshift to the RRM rms measured at 144 MHz for the semi-analytical case and that with density taken from simulations. Columns are the case studied and the fit parameters: the slope α of the filament magnetic field strength behaviour versus redshift; the strength $B_{f,0}$ of the filament magnetic field at $z = 0$; the constant term A_{rrm}; the slope γ of the comoving magnetic field. Semi-analytical cases are with different redshift-bin sizes. Cases with density taken from simulations are all fit to RRMs in 15-source redshift bins and differ for the magnetogenesis scenario and the overdensity threshold of the cells used to estimate the RRMs (matter overdensity $\delta_M < 160$ and $\delta_M < 100$).

Case	α	$B_{f,0}$ (nG)	A_{rrm} (rad m^{-2})	γ
Semi-analytical model, $l_f \propto (1+z)^{-1.4}$				
15-sources per z-bin	0.2 ± 0.5	52 ± 9	0.48 ± 0.16	-1.8 ± 0.5
60-sources per z-bin	-0.8 ± 2.0	80 ± 40	1.0 ± 0.5	-2.8 ± 2.0
Density from simulations, B_f constant with density, 15-source z-bins, $\delta_M < 160$				
density model				
primordial uniform	0.1 ± 0.5	47 ± 8	0.62 ± 0.14	-1.9 ± 0.5
dynamo	-0.1 ± 0.5	56 ± 10	0.49 ± 0.15	-2.1 ± 0.5
astroph	-0.2 ± 0.5	58 ± 11	0.57 ± 0.16	-2.2 ± 0.5
primordial + astroph	0.0 ± 0.5	55 ± 10	0.64 ± 0.13	-2.0 ± 0.5
primordial stochastic	-0.2 ± 0.4	57 ± 9	0.53 ± 0.14	-2.2 ± 0.4
Density from simulations, B_f constant with density, 15-source z-bins, $\delta_M < 100$				
density model				
primordial uniform	0.0 ± 0.5	61 ± 11	0.60 ± 0.14	-2.0 ± 0.5
dynamo	0.0 ± 0.4	65 ± 10	0.57 ± 0.14	-2.0 ± 0.4
astroph	-0.2 ± 0.5	70 ± 14	0.56 ± 0.16	-2.2 ± 0.5
primordial + astroph	-0.1 ± 0.4	69 ± 11	0.59 ± 0.13	-2.1 ± 0.4
primordial stochastic	-0.1 ± 0.6	68 ± 14	0.55 ± 0.16	-2.1 ± 0.6

overdensity assumed to be constant within a filament and for all filaments. To overcome this, and to obtain more precise estimates of the evolution of the field, we make direct use of the gas density from cosmological simulations (see Section 3). The goal is still to find the evolution with redshift of the mean filament magnetic field strength assuming the power-law behaviour of equation (10).

For each of the cosmological models considered, we extracted 100 LOS out to $z = 3$. For each LOS we calculated the RRM$_f$ at each z using equation (3) and the gas density from the simulation. We considered only cells with a matter density excess $\delta_M < 160$ to account for our sources residing far from galaxy clusters. We excluded cells with gas excess density $\delta_g < 1$ because they give a negligible contribution to the total RRM, as shown in Section 4.1.

The magnetic field was estimated assuming a value of $B_{f,0}$ and α (equation 4). Each time the LOS entered a region with $\delta > 1$, the direction of the magnetic field to the LOS was changed, randomly picked within 4π sr. That ensured a magnetic field with constant orientation within each filament and randomly changing filament to filament. We did 120 realizations of these magnetic field configurations, for a total of 12 000 realizations (100 LOS $\times$ 120 magnetic field configurations).

From these 12 000 realizations of RRM$_f$ we computed the RRM$_f$ rms that is that expected given the assumed values of $B_{f,0}$ and α. Since we are not interested to small scale variations, we smoothed the RRM$_f$ rms with a top hat filter of width d$z = 0.1$, which further reduces the statistical variations of the individual RRM$_f$ realizations. We computed this all for different values of α (at the same value of $B_{f,0}$), spanning the range $[-5, 5]$ with steps of 0.5, which covers the range of interest. We also tested a step of 0.25 with similar results. A linear interpolation between the two nearest values gives the RRM$_f$ rms estimate at any other α value. The RRM$_f$ has a simple linear dependence on $B_{f,0}$ that, combined with the interpolation over α, gives us the functional dependence on these two parameters required by a Bayesian fit.

The results of a Bayesian fit to equation (18) are reported in Table 1, with the RRM$_f$ estimated as discussed above, and the RRMs measured in 15-source bins, for all of the cosmological models we considered. We assumed the same priors as for the semi-analytical analysis.

The best-fitting values of α are in the range $[-0.2, 0.1]$ and are all consistent within the errors ($\sigma_\alpha = 0.4$–0.5) and consistent with no evolution with redshift. They are also consistent with the value derived by the semi-analytical analysis. The comoving magnetic field slope γ is in the range $[-2.2, -1.9]$, which confirms a decrement with increasing redshift.

The mean amplitude of the field in a filament at $z = 0$ is $B_{f,0} \approx 55$ nG with variations depending on the models (it ranges from 47–58 nG), but within the uncertainty that is better than 5-sigma. It is consistent with the result of the semi-analytical model.

We regard the results obtained here as more accurate than those of the semi-analytical model, because of the better description of the gas density. However, the proximity of the results tells us that the semi-analytical model is a good approximation and suggests that is an effective (and computationally cheaper) approach to apply to large data sets.

Currently, we cannot exactly set the limit on the overdensity. From the distribution of the source separation to the nearest cluster found in Paper I (see also Section 4.1) it is possible that they reside at overdensities lower than $\delta_M = 160$. Therefore, we repeated the analysis, setting the limit to $\delta_M < 100$, which is the threshold separating filaments and haloes. This is sort of an extreme case because it assumes that all sources are in filaments.

Downloaded from https://academic.oup.com/mnras/article/518/2/2273/6762929 by INAF Trieste (Osservatorio Astronomico di Trieste) user on 30 January 2023

The best-fitting results are reported in Table 1. The slopes are similar to the $\delta_M = 160$ case, with small changes that are well within the uncertainties. However, the field strength is larger. It ranges from 61 to 70 nG, with a mean value of 67 nG. In summary, changing the overdensity limit does not affect the best-fitting slope, while it changes the field amplitude, increasing it by ≈20 per cent when changing from $\delta_M = 160$ to 100. Considering all of the models, overdensity limits, and 1-sigma uncertainties, the magnetic field strength of a filament at $z = 0$ is in the range 39–84 nG.

4.4 Analysis with density from cosmological simulations and magnetic field frozen to matter

The approach used above, in Section 4.3, assumes a B_f which is constant with density. This results in an average value where filaments at higher density contribute more, because the RRM of a filament depends on $\rho_g^{5/3}$.

Therefore, we have repeated the same analysis assuming that the magnetic field strength is

$$B_f = B_{f,0}^{10} \left(\frac{\delta_g}{10}\right)^{2/3} (1+z)^{\alpha}, \tag{21}$$

where $B_{f,0}^{10}$ is the average magnetic field strength of a filament of gas overdensity $\delta_g = 10$ at $z = 0$ and $B_{f,0}^{10}\,(1+z)^{\alpha}$ is that at redshift z. The dependence on δ_g assumes that the magnetic field is frozen to the ionized medium[7] and also seems to hold in more evolved environments like those of galaxy clusters (e.g. Radiconi et al. 2022, submitted). Hence, this approach estimates the field strength at the typical density of a filament ($\delta_g = 10$, see Cautun et al. 2014; Vazza et al. 2015) and, following equation (21), at any density.

The results of the Bayesian fit are given in Table 2 and Fig. B1 of Appendix B (for the primordial stochastic model only, the other models show similar results). The best-fitting values of α are in the range [−0.1, 0.3], are all consistent within the errors (σ_α = 0.4–0.5), and are consistent with no evolution with redshift. The comoving magnetic field slope γ is in the range [− 2.1, −1.7], which gives a decrement with redshift also in this case. The mean amplitude of the field in a filament at overdensity $\delta_g = 10$ and $z = 0$ is $B_{f,0}^{10} \approx 12.3$ nG (values are in the range 10.0–14.2 nG and partly depend on the best-fitting slope – there is some degeneracy between slope and field strength, as shown by Fig. B1), with uncertainties better than 5-sigma.

The typical density of a filament evolves as for equation (4). Combined with our results and the assumed relation of B_f with density, we get that the typical magnetic field of a filament evolves with redshift as $B_{f,t} = B_{f,0}^{10}\,(1+z)^{\eta}$, with $\eta = \alpha - 0.5$ ($\eta_c = \gamma - 0.5$ for the comoving field), that hence runs in the range [−0.6, −0.2] ([−2.6, −2.2] for the comoving field).

As for the case of B_f constant with density, we repeated the analysis for an overdensity limit of $\delta_M = 100$. Results are reported in Table 2. The slopes are similar to the $\delta_M = 160$ case. The magnetic field strength $B_{f,0}^{10}$ ranges from 17 to 22 nG with a mean value of ≈19 nG, which is ≈50 per cent larger than the previous case. Considering all of the models, overdensity limits, and 1-sigma uncertainties, the magnetic field strength of a filament at $z = 0$ and gas overdensity $\delta_g = 10$ is in the range 8–26 nG.

[7] We assume there is no further amplification, such as by turbulent gas motions, which numerical simulations suggest may occur (e.g. Gheller & Vazza 2019).

4.5 Predictions from simulations

It is difficult to discriminate between the different magnetogenesis scenarios based solely on the results of the previous subsections, because those scenarios do not differ much in gas density and give similar outcomes (which, however, gives us a nearly model-independent estimate of the evolution of B_f). However, we can use their directly simulated prediction of the RRM and B_f evolution with redshift.

The RRM$_f$ rms of the IGM were computed for all of the cosmological scenarios following the procedure of Section 4.1, using the density and magnetic field values from the simulations and considering only the LOS cells with an overdensity under a given limit ($\delta_M < 160$ or $\delta_M < 100$). The results are shown in Fig. 6 for both overdensity limits. The RRM rms measured from our sample in 60-source bins, which have lower errors for an easier comparison, is also displayed after subtracting off the term $A_{rrm}(1+z)^{-2}$ to show the component that the fit attributes to the IGM only. We set $A_{rrm} = 0.6$ rad m^{-2} which is an intermediate value of the best-fitting results.

The observed RRMs are best matched in both shape and amplitude (for the $\delta_M = 160$ case) by the dynamo and primordial stochastic models, whose RRM rms flattens at high redshift. The others look disfavoured. In particular, the astrophysical model predicts RRMs that are too small, while the RRM of the mixed primordial uniform + astrophysical and primordial uniform models increases nearly linearly with redshift out to $z = 3$.

The comoving magnetic field strength at $\delta_g = 10$ is estimated as the rms of the magnetic field from cells in the 100 LOS with δ_g in the range 2–50, and is shown in Fig. 7. We also tried narrower ranges, but the statistics were too poor and the results were unstable. Table 3 reports the results of a best fit to a power law $B_{f,c}^{10} = B_{f,0}^{10}\,(1+z)^{\gamma}$. To facilitate the comparison we report the differences with the results of the best fits to the observations for our fiducial overdensity limit of $\delta_M = 160$. Comparisons with the slopes in the case of a limit of $\delta_M = 100$ are similar. The dynamo and primordial stochastic models only posses a comoving slope consistent with the results from the observations. This is not surprising because a steep slope is required to obtain an RRM rms that flattens at high redshift. The magnetic field strength range allowed by the observations is broad. However, the dynamo and primordial stochastic models appear to predict strengths consistent with such a range, albeit the former has a large uncertainty.

5 DISCUSSION

Our analysis indicates that the RRM rms we used is dominated by the component originated in cosmic filaments. We find that the filament physical magnetic field is consistent with no evolution with redshift, regardless of the three types of analysis we have applied and the overdensity limits that we set. The comoving field decreases with redshift with slope $\gamma \approx -2.0 \pm 0.5$, with small variations depending on the magnetogenesis model. This is the first estimate of the evolution of the magnetic field in filaments, to our knowledge, and complements the result by Pomakov et al. (2022) for the average field of the IGM, who find a slope of $\gamma_{\rm IGM} \approx -4.5$. The difference is because in filaments the evolution of their overdensity and transversal size have to be added to the equation, which makes the filaments' γ flatter by 2.15 (see Section 4.2) and the two results consistent. This is the direct result of a nearly flat evolution of RRM that requires a decreasing comoving field.

The strength at $z = 0$ of the filament magnetic field averaged over all filaments is estimated at $B_{f,0} \approx 55$ nG for our fiducial value of the overdensity limit of $\delta_M = 160$, with an uncertainty better than

Downloaded from https://academic.oup.com/mnras/article/518/2/2273/6762929 by INAF Trieste (Osservatorio Astronomico di Trieste) user on 30 January 2023

Table 2. Best-fitting parameters of the filament magnetic field evolution with redshift to the RRM rms measured at 144 MHz for the case with density taken from simulations and magnetic field dependent on the gas density as $B_f \propto \rho_g^{2/3}$. Columns are the case studied and the fit parameters: the slope α of the filament magnetic field behaviour versus redshift; the strength $B^{10}_{f,0}$ of the filament magnetic field at $z = 0$ and gas overdensity $\delta_g = 10$; the constant term A_{rrm}; the slope γ of the comoving magnetic field. All cases are fit to RRM rms computed in 15-source redshift bins and differ for the magnetogenesis scenario. Two sets of cases are reported, differing for the overdensity threshold of the cells used to estimate the RRMs from simulations ($\delta_M < 160$ and $\delta_M < 100$).

Case	α	$B^{10}_{f,0}$ (nG)	A_{rrm} (rad m^{-2})	γ
$B_f \propto \rho_g^{2/3}$, $\delta_M < 160$				
density model				
primordial uniform	0.3 ± 0.5	10.0 ± 2.0	0.70 ± 0.14	-1.7 ± 0.5
dynamo	0.1 ± 0.4	11.8 ± 1.9	0.55 ± 0.15	-1.9 ± 0.4
astroph	-0.1 ± 0.5	12.8 ± 2.4	0.61 ± 0.15	-2.1 ± 0.5
primordial + astroph	-0.1 ± 0.4	12.8 ± 2.1	0.65 ± 0.13	-2.1 ± 0.4
primordial stochastic	-0.1 ± 0.5	14.2 ± 2.6	0.47 ± 0.17	-2.1 ± 0.5
$B_f \propto \rho_g^{2/3}$, $\delta_M < 100$				
density model				
primordial uniform	0.0 ± 0.6	18.0 ± 3.9	0.63 ± 0.16	-2.0 ± 0.6
dynamo	0.1 ± 0.4	18.6 ± 3.1	0.60 ± 0.14	-1.9 ± 0.4
astroph	-0.2 ± 0.5	20.9 ± 3.6	0.57 ± 0.15	-2.2 ± 0.5
primordial + astroph	0.3 ± 0.5	17.2 ± 3.1	0.61 ± 0.14	-1.7 ± 0.5
primordial stochastic	-0.2 ± 0.5	22.4 ± 3.9	0.48 ± 0.15	-2.2 ± 0.5

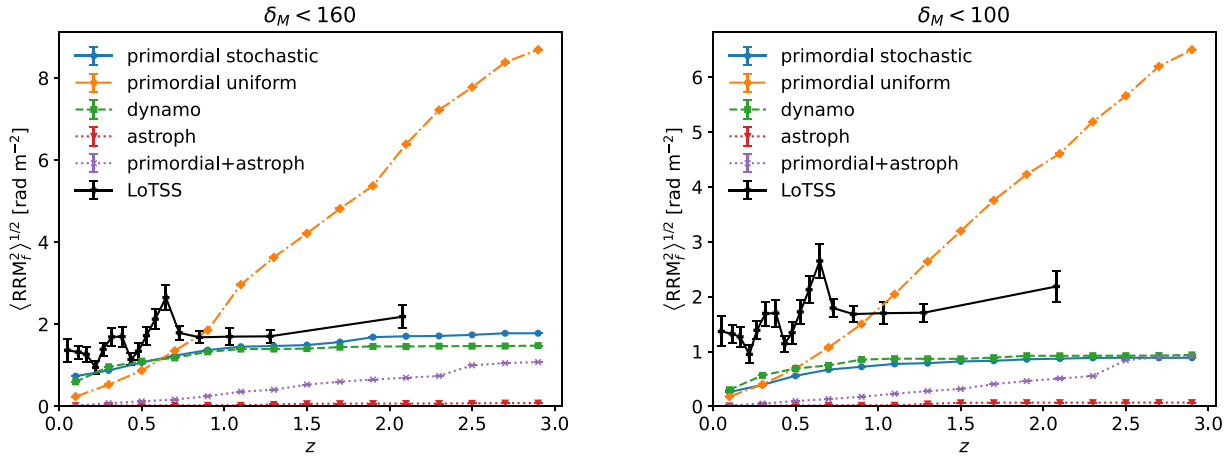


Figure 6. RRM$_f$ rms in redshift bins computed using density and magnetic field from simulations, for the magnetogenesis models we considered. Two cases differing by the overdensity limit are shown: $\delta_M < 160$ (left-hand panel) and $\delta_M < 100$ (right-hand panel). The RRM rms from the LoTSS RM catalogue measured in 60-source redshift bins is also shown, with the term $A_{rrm}(1+z)^{-2}$ subtracted off.

5-sigma. Considering variations due to both overdensity limits, the fit uncertainties, and the different magnetogenesis scenarios, $B_{f,0}$ is in the range 39–84 nG. This result is in agreement both with previous upper limits (Brown et al. 2017; Vernstrom et al. 2017; O'Sullivan et al. 2019; Amaral et al. 2021; Locatelli et al. 2021) and the estimate of[8] 30–60 nG obtained from the first claimed detection of the stacked synchrotron emission from filaments of the cosmic web (Vernstrom et al. 2021). Both our and their method measure the field averaged over all types of filaments and are possibly dominated by the largest of them. Note that our result is larger than that of ≈30 nG derived in Paper I. There we assumed no evolution (with an average filament density at $z = 0.7$) and a filament width constant with redshift (instead of decreasing), which led to a lower field strength estimate. Adding the evolution with redshift was thus essential to get an improved estimate.

We also estimated the magnetic field at the typical filament overdensity of $\delta_g = 10$, finding a strength of $B^{10}_{f,0} \approx 12.3$ nG at $z = 0$ for our fiducial overdensity limit, and a slope with redshift similar to the previous case. If we consider all types of variations (model, overdensity limit, and fit uncertainties) the field strength is in the range 8–26 nG.

[8]It yields ≈60 nG, if equipartition is assumed, or ≈ 30 nG, based on numerical simulations, albeit with a dependence on the (unknown) amount of accelerated radio emitting cosmic ray electron.

Downloaded from https://academic.oup.com/mnras/article/518/2/2273/6762929 by INAF Trieste (Osservatorio Astronomico di Trieste) user on 30 January 2023

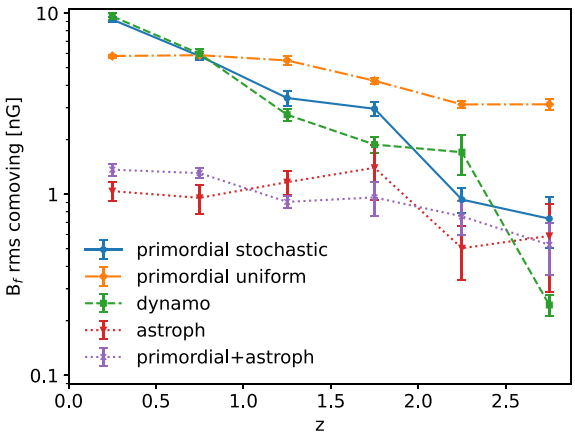


Figure 7. Comoving magnetic field strength at overdensity $\delta_g = 10$ estimated from the simulations of the magnetogenesis models considered in this work.

The dynamo and primordial stochastic models predict RRM rms values that flatten at high redshift and provide the best match to the observed RRM in both shape and amplitude. The others look disfavoured. In particular, the RRM of the primordial uniform model increases almost linearly with redshift and it is striking to notice how such an observed redshift evolution of RRMs clearly disfavours it. While a comoving uniform seed field of $\approx 0.1 - 0.5$ nG was shown to be compatible with previous observations or the non-detection of synchrotron radio emission from the cosmic web (e.g. Vernstrom et al. 2017, 2021; Locatelli et al. 2021) or more local analysis of the RRM (e.g. O'Sullivan et al. 2019), these redshift-dependent constraints on the RRM exclude such a simplistic model of the magnetic field with high confidence. This is because even such a weak 0.1 nG magnetic field correlated on scales as long as the entire tested cosmic volume[9] of $\approx$6 Gpc produces a systematic increase of the RRM with redshift, which is unobserved. This makes the RRM evolution with redshift an extremely powerful probe of cosmic magnetism on cosmic scales.

Furthermore, the comoving magnetic field at $\delta_g = 10$ favours the dynamo and primordial stochastic models, as they are the only models that posses both a comoving slope and strength that are consistent with the results of the best fits to the observations.

The dynamo and primordial stochastic models are thus favoured by our RRM measurements. The primordial uniform, mixed, and astrophysical models appear to be excluded. The former two predict a continuously increasing RRM rms out to $z = 3$. The latter predicts RRMs that are too small and magnetic fields that at $z = 0$ are one order of magnitude weaker than the results of our best fits and a redshift evolution that is too flat. These results are in agreement with Vazza et al. (2021b), who found the stochastic model consistent with previous observational constraints, and Pomakov et al. (2022), who found the dynamo model consistent with the evolution of the mean IGM magnetic field.

Using previous observational constraints, Vazza et al. (2021a) and Vernstrom et al. (2021) also found that the dynamo model is challenged, which, combined with our results, favours the primordial stochastic model only. We note that combinations of the primordial stochastic with other models are possible, but exploring such lines of investigation is beyond the scope of this work.

[9]The initial uniform orientation of the magnetic field is preserved while evolving, on average.

If we restrict the analysis to this most favoured primordial stochastic model, then the filament magnetic field strengths at $z = 0$ are restricted to $B_{f,0} = 48$–82 nG and $B^{10}_{f,0} = 11$–26 nG, while the slopes are $\alpha = -0.15 \pm 0.5$ and $\gamma = -2.15 \pm 0.5$.

The RRM rms amplitude of the primordial stochastic scenario depends linearly on the initial field strength $B_{\rm Mpc}$. A best fit of the amplitude of the directly simulated RRM rms of Fig. 6 to the observed RRM rms gives the value that is most consistent with our data. We found that it is $B_{\rm Mpc} = 0.051 \pm 0.010$ nG and 0.097 ± 0.010 nG, comoving, for overdensity limits of $\delta_M = 160$ and 100, respectively. We restricted the fit to the values at $z > 1$ because they are least affected by the $A_{rrm}\,(1+z)^{-2}$ correction term. A range of $B_{\rm Mpc} = 0.04$–0.11 nG, comoving, thus best matches the RRMs of our sample, for a primordial stochastic scenario with a spectrum of slope $\alpha_s = 1$, which we simulated. These results are consistent with previous upper limits of 0.12–0.13 nG derived from CMB observations for the same scenario (Paoletti & Finelli 2019; Paoletti et al. 2022).

It is worth noting that the mass resolution of the simulations we ran does not allow us to reproduce the total distribution of low mass galaxies (e.g. dwarf galaxies), which can introduce an additional magnetization baseline even in voids (e.g. Beck et al. 2013). Simulations with higher resolution and adaptive mesh that are better suited to resolve the formation of small galaxies in voids predict the formation of 'magnetization bubbles'. These bubbles typically have $\geq 10^{-3}$ nG fields, yet with volume filling factors and magnetization amplitudes from dwarf galaxies that depend on the assumed input magnetic field (Arámburo-García et al. 2021), which currently has an unclear contribution to the observed RRM (Aramburo-Garcia et al. 2022). Higher resolution simulations are thus required in future work to complete the assessment of the astrophysical scenario, although the magnetic field strength at $\delta_g = 10$ in such high resolution simulations is comparable to the ≈ 1 nG that we find in ours (Fig. 7, see also fig. 2 of Pomakov et al. 2022) and large variations from our results are not expected.

6 CONCLUSIONS

We estimated the extragalactic RM contribution (RRM) of the RM catalogue derived from LoTSS DR2 survey data, and, following the procedure of Paper I, measured their rms in redshift bins of sources out to $z = 3$. We used the RRM rms to investigate the evolution with redshift of the magnetic field strength in cosmic web filaments. Our main findings are:

(i) The RRM component that originates local to the source contributes only $\approx$8 per cent to the total RRM. Using cosmological simulations, we also found that voids are expected to have a marginal contribution to the total RRM from the IGM. The polarized radiation from our sample at 144 MHz tends to avoid intervening galaxy clusters along the line of sight. Cosmic filaments are hence the dominant term of our observed RRMs measured at 144 MHz.

(ii) Adding an error term to account for the small local origin component, we used densities from cosmological MHD simulations of five different magnetogenesis scenarios to fit a physical magnetic field in cosmic filaments of shape $B_f = B_{f,0}\,(1+z)^{\alpha}$ to the measured RRM rms. We also allowed an additional constant term evolving with redshift. In the cases where we fit a mean magnetic field, we find the slope is in the range $\alpha = [-0.2, 0.1]$, depending on the scenario, with an error of $\sigma_\alpha = 0.4$–0.5, which is consistent with no evolution. The comoving field has slope $\gamma = [-2.2, -1.9]$, which means that it decreases at high significance. This is as a consequence of the nearly flat behaviour of the RRM rms. The strength at $z = 0$ is

Downloaded from https://academic.oup.com/mnras/article/518/2/2273/6762929 by INAF Trieste (Osservatorio Astronomico di Trieste) user on 30 January 2023

Table 3. Results of the power-law best fit to the comoving magnetic field at $\delta_g = 10$ for all of the cosmological models we considered. The power law is $B^{10}_{f,c} = B^{10}_{f,0}\,(1+z)^{\gamma}$ and the columns are: model; best fit of the slope γ and amplitude $B^{10}_{f,0}$ (field strength at $z = 0$ and $\delta_g = 10$); difference between these best-fitting values and those from the fit to the observations in Table 2 in the case of an overdensity threshold of $\delta_M < 160$ ($\Delta\gamma$ and $\Delta B^{10}_{f,0}$).

Model	γ	$B^{10}_{f,0}$ (nG)	$\Delta\gamma$	$\Delta B^{10}_{f,0}$ (nG)
Primordial uniform	-0.6 ± 0.2	7.7 ± 1.2	1.1 ± 0.5	-2 ± 2
Dynamo	-2.8 ± 0.7	25 ± 15	-0.9 ± 0.8	13 ± 15
Astroph	-0.5 ± 0.4	1.4 ± 0.5	1.6 ± 0.6	-11 ± 2
Primordial + astroph	-0.8 ± 0.2	1.8 ± 0.3	1.3 ± 0.4	-11 ± 2
Primordial stochastic	-2.3 ± 0.4	20 ± 7	-0.2 ± 0.6	6 ± 7

in the range $B_{f,0} = 39$–84 nG and is consistent with previous results based on synchrotron emission stacking.

(iii) If we assume that the magnetic field depends on the gas density as $B_f \propto \rho_g^{2/3}$ (i.e. frozen to the plasma), the slopes are mostly similar to the previous case and the strength, at $z = 0$ and at an overdensity of $\delta_g = 10$ that is typical of filaments, is $B^{10}_{f,0} = 8$–26 nG.

(iv) Comparing the RRM rms and $B^{10}_{f,0}$ predicted by the five simulated scenarios with those from our measurements and best fits, leads to the dynamo and primordial stochastic models being favoured, mainly because of the flat RRM rms they predict. The primordial uniform, astrophysical, and mixed models appear to be rejected, in particular the former is disfavoured by its RRM rms that is continuously increasing with redshift. The strong rejection of the simple primordial uniform model is a new result that is mostly due to the constraints from the evolution with redshift of the RRM rms. Considering earlier work also, only the primordial stochastic scenario (with a spectrum of slope $\alpha_s = 1$) is favoured. Its best-fitting slope is $\alpha = -0.15 \pm 0.5$. The comoving field slope is $\gamma = -2.15 \pm 0.5$. The best-fitting value of the initial field is $B_{\rm Mpc} = 0.04$–0.11 nG.

This work has provided a first advance of our initial analysis conduced in Paper I and has led us to estimating the behaviour with redshift of the magnetic field in cosmic web filaments. This has thus also provided a more accurate estimate of the field strength. We find that the physical field is consistent with no evolution and the comoving field decreases with redshift with a slope $\gamma \approx -2.0 \pm 0.5$ (-2.15 ± 0.5 for the most favoured scenario). Such a result is because of the nearly flat RRM rms behaviour with redshift, and has important implications on understanding what process has generated magnetic fields in the Universe and how they have evolved. A primordial field with a uniform initial field is unsuitable. A primordial field with random stochastic initial conditions is favoured and we find a range of initial field strengths that best match our data.

Further advances can be pursued with future work and data. An improvement of a factor of three of the RRM rms uncertainties, which could be reached with 9× more sources, would give errors on α of ≈0.15, significantly improving the precision. This is within the reach of the full LoTSS survey that will have larger area (4×), better resolution (6 versus 20 arcsec), and improved polarized source selection (see discussion in O'Sullivan et al., submitted). ASKAP-POSSUM (Gaensler et al. 2010), APERTIF (Adebahr et al. 2022), and SKA-LOW (Braun et al. 2019) will be a further step ahead. A functional description of the evolution of B_f that is more sophisticated than the simple power law assumed here is a further improvement to pursue, even though it would likely be model dependent – see Fig. 7. A better separation of the IGM from the local origin component is desirable, to improve the estimate of the IGM RRM rms, which can be done with component separation Bayesian algorithms (Vacca et al. 2016).

ACKNOWLEDGEMENTS

We thank an anonymous reviewer for helpful comments that helped us improve the paper. This work has been conducted within the LOFAR Magnetism Key Science Project[11] (MKSP). This work has made use of LoTSS DR2 data (Shimwell et al. 2022). EC and VV acknowledge this work has been conducted within the INAF program METEORA. VV acknowledges support from Istituto Nazionale di Astrofisica (INAF) mainstream project 'Galaxy Clusters Science with LOFAR' 1.05.01.86.05. FV acknowledges financial support from the H2020 StG MAGCOW (714196). AB acknowledges support from ERC Stg DRANOEL n. 714245 and MIUR FARE grant 'SMS'. In this work we used the ENZO code (http://enzo-project.org), the product of a collaborative effort of scientists at many universities and national laboratories. Our simulations were run on the JUWELS cluster at Juelich Superc omputing Centre (JSC), under project 'radgalicm2', and on the Piz Daint supercomputer at CSCS-ETHZ (Lugano, Switzerland), under project s1096, in both cases as FV as a Principal Investigator. LOFAR (van Haarlem et al. 2013) is the Low Frequency Array designed and constructed by ASTRON. It has observing, data processing, and data storage facilities in several countries, which are owned by various parties (each with their own funding sources), and which are collectively operated by the ILT foundation under a joint scientific policy. The ILT resources have benefited from the following recent major funding sources: INSU, CNRS, Observatoire de Paris and Université d'Orléans, France; BMBF, MIWF-NRW, MPG, Germany; Science Foundation Ireland (SFI), Department of Business, Enterprise and Innovation (DBEI), Ireland; NWO, The Netherlands; The Science and Technology Facilities Council, UK; Ministry of Science and Higher Education, Poland; The Istituto Nazionale di Astrofisica (INAF), Italy. LoTSS made use of the Dutch national e-infrastructure with support of the SURF Cooperative (e-infra 180169) and the LOFAR e-infra group. The Jülich LOFAR Long Term Archive and the German LOFAR network are both coordinated and operated by the Jülich Supercomputing Centre (JSC), and computing resources on the supercomputer JUWELS at JSC were provided by the Gauss Centre for Supercomputing e.V. (grant CHTB00) through the John von Neumann Institute for Computing (NIC). LoTSS made use of the

[11] https://lofar-mksp.org/

Downloaded from https://academic.oup.com/mnras/article/518/2/2273/6762929 by INAF Trieste (Osservatorio Astronomico di Trieste) user on 30 January 2023

University of Hertfordshire high-performance computing facility and the LOFAR-UK computing facility located at the University of Hertfordshire and supported by STFC [ST/P000096/1], and of the Italian LOFAR IT computing infrastructure supported and operated by INAF, and by the Physics Department of Turin university (under an agreement with Consorzio Interuniversitario per la Fisica Spaziale) at the C3S Supercomputing Centre, Italy. This work made use of the Python packages NUMPY (Harris et al. 2020), ASTROPY (Astropy Collaboration 2013), MATPLOTLIB (Hunter 2007), and EMCEE (Foreman-Mackey et al. 2013). Some of the results in this paper have been derived using the HEALPY (Zonca et al. 2019) and HEALPIX[12] (Górski et al. 2005) packages.

DATA AVAILABILITY

The LoTSS DR2 RM catalogue will be publicly released as the paper describing it (O'Sullivan et al., submitted) will be accepted for publication. The cosmological simulations of this project have been produced with the public code ENZO.[10] Examples of the simulated data sets can be found at this URL: https://cosmosimfrazza.myfreesites.net/scenarios-for-magnetogenesis.

REFERENCES

Adebahr B. et al., 2022, A&A, 663, A103
Amaral A. D., Vernstrom T., Gaensler B. M., 2021, MNRAS, 503, 2913
Aragón-Calvo M. A., van de Weygaert R., Jones B. J. T., 2010, MNRAS, 408, 2163
Arámburo-García A., Bondarenko K., Boyarsky A., Nelson D., Pillepich A., Sokolenko A., 2021, MNRAS, 505, 5038
Aramburo-Garcia A., Bondarenko K., Boyarsky A., Neronov A., Scaife A., Sokolenko A., 2022, preprint (arXiv:2204.06475)
Astropy Collaboration 2013, A&A, 558, A33
Beck A. M., Hanasz M., Lesch H., Remus R. S., Stasyszyn F. A., 2013, MNRAS, 429, L60
Bertone S., Vogt C., Enßlin T., 2006, MNRAS, 370, 319
Bonafede A. et al., 2022, ApJ, 933, 218
Bosman S. E. I. et al., 2022, MNRAS, 514, 55
Botteon A. et al., 2020, MNRAS, 499, L11
Braun R., Bonaldi A., Bourke T., Keane E., Wagg J., 2019, preprint (arXiv:1912.12699)
Brentjens M. A., de Bruyn A. G., 2005, A&A, 441, 1217
Brown S. et al., 2017, MNRAS, 468, 4246
Brown S., Rudnick L., 2011, MNRAS, 412, 2
Burn B. J., 1966, MNRAS, 133, 67
Carretti E. et al., 2022, MNRAS, 512, 945 (Paper I)
Carrón Duque J., Migliaccio M., Marinucci D., Vittorio N., 2022, A&A, 659, A166
Cautun M., van de Weygaert R., Jones B. J. T., Frenk C. S., 2014, MNRAS, 441, 2923
Chen Y.-C., Ho S., Brinkmann J., Freeman P. E., Genovese C. R., Schneider D. P., Wasserman L., 2016, MNRAS, 461, 3896
de Gasperin F. et al., 2022, A&A, 659, A146
Dickey J. M. et al., 2022, preprint (arXiv:2209.10819)
Foreman-Mackey D., Hogg D. W., Lang D., Goodman J., 2013, PASP, 125, 306
Gaensler B. M., Landecker T. L., Taylor A. R., POSSUM Collaboration, 2010, American Astronomical Society Meeting Abstracts #215, 470.13
Galárraga-Espinosa D., Aghanim N., Langer M., Gouin C., Malavasi N., 2020, A&A, 641, A173
Gheller C., Vazza F., 2019, MNRAS, 486, 981
Górski K. M., Hivon E., Banday A. J., Wandelt B. D., Hansen F. K., Reinecke M., Bartelmann M., 2005, ApJ, 622, 759
Govoni F. et al., 2019, Science, 364, 981
Harris C. R. et al., 2020, Nature, 585, 357
Hunter J. D., 2007, Comput. Sci. Eng., 9, 90
Hutschenreuter S. et al., 2022, A&A, 657, A43
Jansson R., Farrar G. R., 2012, ApJ, 757, 14
Kim K. T., Kronberg P. P., Giovannini G., Venturi T., 1989, Nature, 341, 720
Klypin A. A., Trujillo-Gomez S., Primack J., 2011, ApJ, 740, 102
Kronberg P. P., 1994, Rep. Progr. Phys., 57, 325
Kronberg P. P., Bernet M. L., Miniati F., Lilly S. J., Short M. B., Higdon D. M., 2008, ApJ, 676, 70
Laing R. A., Bridle A. H., Parma P., Murgia M., 2008, MNRAS, 391, 521
Locatelli N., Vazza F., Bonafede A., Banfi S., Bernardi G., Gheller C., Botteon A., Shimwell T., 2021, A&A, 652, A80
Mtchedlidze S., Domínguez-Fernández P., Du X., Brandenburg A., Kahniashvili T., O'Sullivan S., Schmidt W., Brüggen M., 2022, ApJ, 929, 127
O'Sullivan S. P. et al., 2019, A&A, 622, A16
O'Sullivan S. P. et al., 2020, MNRAS, 495, 2607
Paoletti D., Chluba J., Finelli F., Rubiño-Martin J. A., 2022, preprint (arXiv:2204.06302)
Paoletti D., Finelli F., 2019, J. Cosmol. Astropart. Phys., 2019, 028
Planck Collaboration XIII 2016, A&A, 594, A13
Pomakov V. P. et al., 2022, MNRAS, 515, 256
Porayko N. K. et al., 2019, MNRAS, 483, 4100
Radiconi F. et al., 2022, preprint (arXiv:2206.04697)
Reiprich T. H., Basu K., Ettori S., Israel H., Lovisari L., Molendi S., Pointecouteau E., Roncarelli M., 2014, in Ishida M., Petre R., Mitsuda K., eds, Suzaku-MAXI 2014: Expanding the Frontiers of the X-ray Universe. Ehime University, Matsuyama, Japan, p. 362
Ryu D., Kang H., Cho J., Das S., 2008, Science, 320, 909
Shimwell T. W. et al., 2017, A&A, 598, A104
Shimwell T. W. et al., 2019, A&A, 622, A1
Shimwell T. W. et al., 2022, A&A, 659, A1
Sotomayor-Beltran C. et al., 2013, A&A, 552, A58
Stuardi C. et al., 2020, A&A, 638, A48
Subramanian K., 2016, Rep. Progr. Phys., 79, 076901
Turner M. S., Widrow L. M., 1988, Phys. Rev. D, 37, 2743
Vacca V. et al., 2016, A&A, 591, A13
Vacca V. et al., 2018, MNRAS, 479, 776
van Haarlem M. P. et al., 2013, A&A, 556, A2
Vazza F. et al., 2021a, Galaxies, 9, 109
Vazza F., Brüggen M., Gheller C., Hackstein S., Wittor D., Hinz P. M., 2017, Class. Quantum Gravity, 34, 234001
Vazza F., Ferrari C., Brüggen M., Bonafede A., Gheller C., Wang P., 2015, A&A, 580, A119
Vazza F., Paoletti D., Banfi S., Finelli F., Gheller C., O'Sullivan S. P., Brüggen M., 2021b, MNRAS, 500, 5350
Venturi T., et al. 2022, A&A , 660, A81
Vernstrom T., Gaensler B. M., Brown S., Lenc E., Norris R. P., 2017, MNRAS, 467, 4914
Vernstrom T., Gaensler B. M., Rudnick L., Andernach H., 2019, ApJ, 878, 92
Vernstrom T., Heald G., Vazza F., Galvin T. J., West J. L., Locatelli N., Fornengo N., Pinetti E., 2021, MNRAS, 505, 4178
Wen Z. L., Han J. L., 2015, ApJ, 807, 178
Xu J., Han J. L., 2014, MNRAS, 442, 3329
Xu J., Han J. L., 2022, ApJ, 926, 65
Zonca A., Singer L., Lenz D., Reinecke M., Rosset C., Hivon E., Gorski K., 2019, J. Open Source Softw., 4, 1298

APPENDIX A: RELATION BETWEEN 2D AND 3D PROBABILITIES OF FINDING A SOURCE CLOSER THAN A DISTANCE

Assuming that a 3D probability distribution F is the same along all of the directions: $F(x, y, z) = f((x)f(y)f(z)$, in first approximation, the

[12] http://healpix.sf.net
[10] http://enzo-project.org

Downloaded from https://academic.oup.com/mnras/article/518/2/2273/6762929 by INAF Trieste (Osservatorio Astronomico di Trieste) user on 30 January 2023

3D probability that the variable is within a distance d from the centre on each direction is:

$$p_{3D}(d) = \int_{-d}^{d} f(x)\mathrm{d}x \int_{-d}^{d} f(y)\mathrm{d}y \int_{-d}^{d} f(z)\mathrm{d}z \quad \text{(A1)}$$

$$= p_{1D}^{3}(d) \quad \text{(A2)}$$

where

$$p_{1D}(d) = \int_{-d}^{d} f(z)\mathrm{d}z. \quad \text{(A3)}$$

This is only a first approximation because the integration should not be extended out to d in all directions. The correct p_{3D} is thus smaller.

Marginalizing in the direction z, we obtain the 2D probability that the variable is within a distance d along two directions only:

$$p_{2D}(d) = \int_{-d}^{d} f(x)\mathrm{d}x \int_{-d}^{d} f(y)\mathrm{d}y \int_{-\infty}^{\infty} f(z)\mathrm{d}z \quad \text{(A4)}$$

$$= p_{1D}^{2}(d) \quad \text{(A5)}$$

This also is an approximation.

Hence,

$$p_{3D}(d) \approx p_{2D}^{3/2}(d) \quad \text{(A6)}$$

APPENDIX B: BEST FIT OF RRM ASSUMING THE MAGNETIC FIELD FROZEN TO THE PLASMA

Best-fitting results of equation (18) to the measured RRM rms, for the case in which the magnetic field is assumed to be frozen to the plasma, are shown in Fig. B1. Only the case of the primordial stochastic scenario is shown.

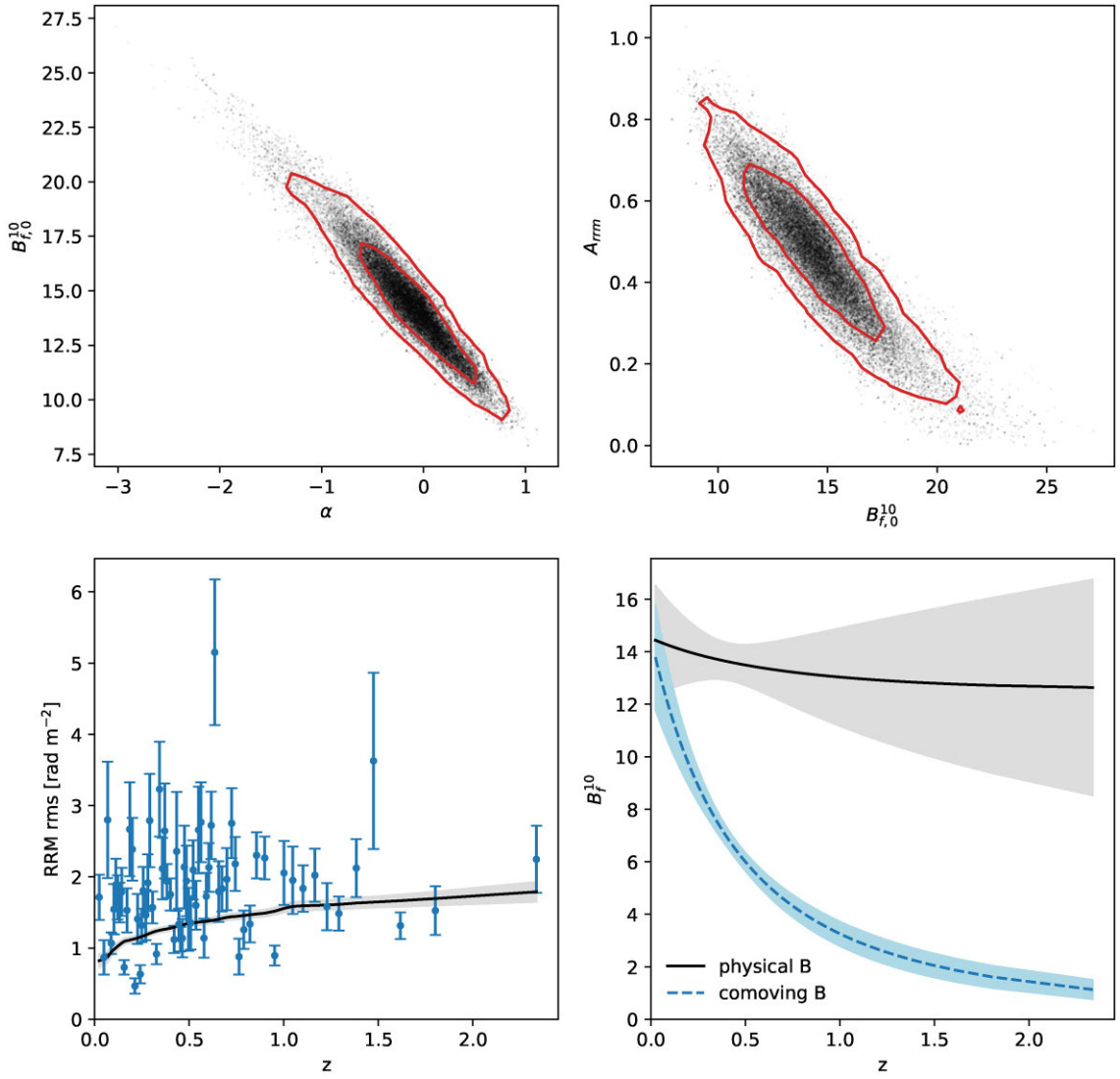


Figure B1. Best-fitting results of equation (18) to the RRM rms measured with redshift bins of 15 sources each. The filament RRM$_f$ is computed from equation (3), where the density is taken from cosmological simulations and the magnetic field strength depends on the gas density as $B_f \propto \rho_g^{2/3}$. The overdensity limit assumed is $\delta_M < 160$. The case of the primordial stochastic cosmological MHD model is shown here. The description of the panels is as for Fig. 5.

This paper has been typeset from a TEX/LATEX file prepared by the author.

Downloaded from https://academic.oup.com/mnras/article/518/2/2273/6762929 by INAF Trieste (Osservatorio Astronomico di Trieste) user on 30 January 2023